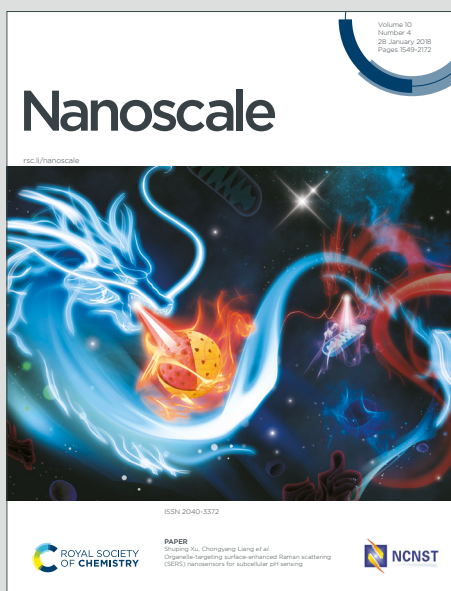


# Nanoscale

Accepted Manuscript

This article can be cited before page numbers have been issued, to do this please use: J. Spièce, C. Evangelì, A. J. Robson, A. El Sachat, L. Haenel, M. I. Alonso, M. Garriga, B. J. Robinson, M. Oehme, J. Schulze, F. Alzina, C. M. Sotomayor Torres and O. V. Kolosov, *Nanoscale*, 2021, DOI: 10.1039/D0NR08768H.



This is an Accepted Manuscript, which has been through the Royal Society of Chemistry peer review process and has been accepted for publication.

Accepted Manuscripts are published online shortly after acceptance, before technical editing, formatting and proof reading. Using this free service, authors can make their results available to the community, in citable form, before we publish the edited article. We will replace this Accepted Manuscript with the edited and formatted Advance Article as soon as it is available.

You can find more information about Accepted Manuscripts in the [Information for Authors](#).

Please note that technical editing may introduce minor changes to the text and/or graphics, which may alter content. The journal's standard [Terms & Conditions](#) and the [Ethical guidelines](#) still apply. In no event shall the Royal Society of Chemistry be held responsible for any errors or omissions in this Accepted Manuscript or any consequences arising from the use of any information it contains.

## ARTICLE

# Quantifying thermal transport in buried semiconductor nanostructures via Cross-Sectional Scanning Thermal Microscopy

Received 00th January 20xx,  
Accepted 00th January 20xx

DOI: 10.1039/x0xx00000x

Jean Spìèce,<sup>\*a</sup> Charalambos Evangelis,<sup>a,†</sup> Alexander J. Robson,<sup>a</sup> Alexandros El Sachat,<sup>b</sup> Linda Haenel,<sup>e</sup> M. Isabel Alonso,<sup>c</sup> Miquel Garriga,<sup>c</sup> Benjamin J. Robinson,<sup>a,d</sup> Michael Oehme,<sup>e</sup> Jörg Schulze,<sup>e</sup> Francesc Alzina,<sup>b</sup> Clivia Sotomayor Torres,<sup>b,f</sup> and Oleg V. Kolosov<sup>\*c,d</sup>

Managing thermal transport in nanostructures became a major challenge in development of active microelectronic, optoelectronic and thermoelectric devices, stalling the famous Moore's law of clock speed increase of microprocessors for more than a decade. To find the solution to this and linked problems, one needs to quantify the ability of these nanostructures to conduct the heat, with adequate precision, nanoscale resolution and, essentially, for the internal layers buried in the 3D structure of modern semiconductor devices. Existing thermoreflectance measurements and "hot wire" 3w methods cannot be effectively used at lateral dimensions of the layer below a micrometre, moreover, they are sensitive mainly to the surface layers of a relatively high thickness of above 100 nm. The scanning thermal microscopy (SThM) while providing required lateral resolution, provides mainly qualitative data of the layer conductance due to undefined tip-surface and interlayer contact resistances. In this work, we use cross-sectional SThM (xSThM), a new method combining a scanning probe microscopy compatible Ar-ion beam exit nano-cross-sectioning (BEXP) and SThM, to quantify thermal conductance in complex multilayer nanostructures and to measure local thermal conductivity of oxide and semiconductor materials such as SiO<sub>2</sub>, SiGe<sub>x</sub> and GeSn<sub>y</sub>. By using the new method that provides 10 nm thickness and few tens of nm lateral resolution, we pinpoint crystalline defects in SiGe/GeSn optoelectronic materials by measuring nanoscale thermal transport and quantifying thermal conductivity and interfacial thermal resistance in thin spin-on materials used in Extreme ultraviolet lithography (eUV) fabrication processing. The new capability of xSThM demonstrated here for the first time is poised to provide vital insights for thermal transport in advanced nanoscale materials and devices.

## Introduction

Nanomanufacturing that became a major foundation for modern technological development directly relies on rapid and versatile quantitative characterization of devices on the nanoscale. While scanning and transmission electron microscopies (SEM and TEM) provide excellent nanostructural characterization, the means for mapping of materials and devices specific physical properties are lagging well behind. In particular, one of the most vital characteristics of materials at

the nanoscale, their ability to transfer or impede heat, is also one of the most difficult to characterize. The microelectronic industry is struggling to dissipate heat generated by nanoscale hot spots in computer processor chips,<sup>1, 2</sup> the new nanostructured thermoelectrics rely on suppressing the detrimental thermal conductance pathways, and phase change memory that strive to replace both flash and dynamic memory, need improved management of the local heat generation to become a feasible alternative.<sup>3</sup>

However, measurement of thermal conductivity, even in a simple geometry such as a thin film on a substrate, presents significant challenges to traditional techniques if the layer thickness is smaller than 100 nm.<sup>4</sup> In particular, decoupling the thermal conductivity and the interfacial resistance between the film and the substrate, and accessing the in-plane thermal conductivity is difficult and often not possible.<sup>5</sup> Furthermore, as nanostructured device architectures are becoming more complex, with increased layer number and innovative three-dimensional (3D) geometries such as FIN-FET transistors and low-k interconnects, new approaches are required to probe thermal transport in buried layers and the interlayer interfaces. Existing techniques are mostly limited to either surface or bulk

<sup>a</sup> Physics Department, Lancaster University, LA1 4YB, UK. E-mail: o.kolosov@lancaster.ac.uk, spiece.jean@gmail.com

<sup>b</sup> Catalan Institute of Nanoscience and Nanotechnology (ICN2), CSIC and BIST, Campus UAB, Bellaterra, 08193 Barcelona, Spain.

<sup>c</sup> Institut de Ciència de Materials de Barcelona (ICMAB-CSIC), Campus UAB, 08193 Bellaterra, Spain.

<sup>d</sup> Material Science Institute, Lancaster University, Lancaster, LA1 4YB, UK

<sup>e</sup> University of Stuttgart, Pfaffenwaldring 47, 70569 Stuttgart, Germany

<sup>f</sup> ICREA, Passeig Lluís Companys 23, E-08010 Barcelona, Spain.

<sup>†</sup> Current address: Department of Materials, University of Oxford, Oxford, OX1 3PH, UK.

Electronic Supplementary Information (ESI) available: [details of any supplementary information available should be included here]. See DOI: 10.1039/x0xx00000x

probing and cannot assess thermal transport in buried nanostructures.

Scanning probe microscopy (SPM) based techniques such as scanning thermal microscopy (SThM) could provide an efficient solution, with lateral resolution on the order of few nm to few tens of nm.<sup>6,7</sup> SThM uses a probe with a heated thermal sensor and nanoscale sharp apex that is brought in thermal contact with the sample and scanned in a raster pattern over the surface of the probed sample. The electrical resistance of the probe sensor is proportional to its temperature and is monitored during the scan. By measuring probe temperature, heat transfer properties of the sample can be deduced.<sup>8-10</sup> However, whilst using SThM to quantify overall thermal conductance of the complex 3D structure remains challenging but possible, assessing thermal conductivities of the individual structure elements buried in the 3D device and reliably separating it from the interfacial thermal resistance remains out of reach of the technique. Several groups<sup>11-16</sup> devoted their studies to temperature and conductance measurements using SThM. While Park *et al.*<sup>13</sup> reported measurements of ErAs/GaAs MBE superlattices with 6 nm RMS roughness, Juszcyk *et al.*<sup>14</sup> used craters in photonic structures to access subsurface materials. If the structure allows cleavage, such as in coherent crystalline materials, these can be probed as demonstrated by Jung *et al.*<sup>15</sup> where LED cleavage was used to map nanoscale temperature distribution during its operation. However, all the methods reported lack reproducibility, can only be used to study a small set of structures, and most prominently use ill-defined surfaces, which creates major hurdles for SThM probe measurements.

To address these challenges, here we demonstrate cross-sectional SThM (xSThM), a new method, which combines SThM with beam-exit nano-cross-sectional polishing (BEXP), a nano-cross-sectioning tool, that creates an easily accessible close to atomically flat section through a 3D structure enabling SPM analysis of subsurface layers of the studied material or device.<sup>17,18</sup> The cross-sectioned surface has wedge-like geometry and sub-nm surface roughness and is fully compatible with SThM enabling thermal transport measurements as a function of material thickness that changes depending on the position of the probe across the cut.

We demonstrate the capabilities of this new method by exploring the heat transport in complex buried semiconductor and optoelectronic nanostructures, quantifying the nanoscale gradients in composition and revealing dislocations and defects via variation in the local heat conductance. Furthermore, by analyzing the SThM signal of the wedge-shaped section, and applying an appropriate analytical model, we independently extract the intrinsic thermal conductivity of isotropic material layers on a substrate. The ease of use of our approach and extreme sensitivity to physical properties renders it suitable for a broad range of samples and opens new paths for fundamental and applied research in nanomaterials and devices.

## Experimental

### SThM Compatible Nano-Cross-sectioning

The nano-cross-sectioning (see Fig. 1a) described elsewhere<sup>19,20</sup> has been used to create an easily accessible surface through a 3D structure for subsurface SPM analysis of the material.<sup>17,18</sup> Briefly, it uses three intersecting Ar-ion beams aligned to a single plane that impinge on a sample side at a small negative angle ( $\sim -5^\circ$ ) from below the sample surface. As the beam exits at a glancing angle to the sample surface, we call this technique beam-exit nano-cross-sectional polishing.<sup>18,21</sup> The cross-sectioned surface obtained has a wedge-like geometry and sub-nm surface roughness making it fully compatible for studies via SPM methods. Equally essential, the glancing angle of the ion beam and the inert nature of Ar results in negligible surface damage and practically no modification of the measured physical properties of studied materials.

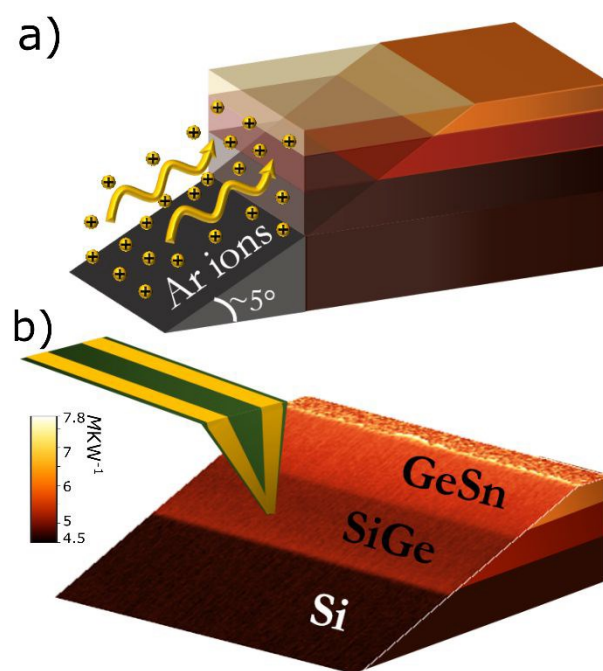


**Fig. 1.** (a) Schematic representation of nano-cross-sectioning beam-exit cross-section polishing (BEXP); Ar ions impinge on the sample edge at a shallow negative angle (ca.  $-5^\circ$ ) to its surface creating a SPM compatible cut adjacent to the intact sample surface. (b) Schematic representation of the xSThM measurement; SThM probe scans the cross-sectioned area of a multilayered material (The sample is presented in the next section). The 3D topography is overlaid with SThM response. Image dimensions:  $5 \times 5 \times 0.77 \mu\text{m}$ .

The cross-sectioned area is then thermally imaged via SThM (see Fig. 1b). Here, SThM measurements were performed in an ambient environment using a commercial SPM (Bruker MultiMode Nanoscope IIIa controller) and custom-built electronics. Acting as both a sensor and a heater, the SThM probe (Kelvin Nanotechnology, KNT-SThM-01a, 0.3 N/m spring constant, <100 nm tip radius) is based on a SiN cantilever with gold legs connecting a Pd film evaporated on the tip.<sup>22</sup> The SThM probe is one of the Wheatstone bridge resistors thus allowing precise monitoring of the probe resistance as explained elsewhere.<sup>7</sup> In this work, we used an excess temperature of 50K with respect to the environment. When scanning across the sample the surface, the probe is biased by a combined AC+DC voltage and its resistance is monitored *via* a modified Wheatstone bridge.<sup>23</sup> When the SThM probe at temperature difference  $\Delta T$  above sample temperature contacts the sample surface, cools down depending on the heat flux  $q$  to the sample and, consequently, on the sample local heat transport characteristics. These temperature variations change the electrical resistance of the probe which is quantified via calibration techniques described elsewhere<sup>7, 24</sup> and used to determine the sample thermal properties. By measuring  $q$  and  $\Delta T$ , the tip-sample thermal contact resistance  $R_X = \Delta T/q$  can be found. To achieve that, we process the acquired data using a calibration methodology that provides compensation for the tip geometry and ambient air conductance<sup>25</sup> and more importantly gives comparable quantitative measurements with ones performed in high vacuum environment (see Supporting Information for details).

## Results and Discussion

### Measuring anisotropic thermal conductance on the Nanoscale

In this section, we use the new method to investigate nanoscale transport in complex anisotropic systems with the predominantly diffusive thermal transport and qualitatively compare thermal conductivities in such layers. Fig. 1b shows a 3D topography rendering section that is overlaid with color corresponding to the SThM output of an MBE grown multilayer sample of Si/Si<sub>x</sub>Ge<sub>1-x</sub>/Ge/Ge<sub>y</sub>Sn<sub>1-y</sub>. The GeSn materials represent a potential platform for Si manufacturing-based optoelectronics due to possibility of achieving direct bandgap.<sup>26-28</sup> In this structure, first a 100 nm Ge layer was grown on a silicon substrate. During the growth Si atoms diffuse inside the Ge layer at high process temperatures<sup>29</sup> and therefore create SiGe alloy of decreasing Si concentration as distance from Si-Ge interface increases (see Supporting Information for details). Then, another 100 nm Ge layer is grown creating a so-called Ge “virtual substrate”. Finally, 200 nm of Ge<sub>0.9</sub>Sn<sub>0.1</sub> are grown on the top of this layer. The z-gradient in the Si<sub>x</sub>Ge<sub>1-x</sub> and Ge<sub>y</sub>Sn<sub>1-y</sub> layer breaks the isotropic nature of the sample making it transversely isotropic. The three regions corresponding to the Si substrate, the Ge virtual substrate and the Ge<sub>0.9</sub>Sn<sub>0.1</sub> layer are clearly observed in the thermal image. Fig. 2b shows the dependence of  $R_X$  and topography profile  $x$  as a function of height,  $t$ , of the sample nano-cross-section as obtained from a

profile of the xSThM image (Fig. 2a) and the topography image respectively. The height is quantified via topography since the thickness of the layer varies linearly with the position.<sup>21</sup> The relatively low constant thermal resistance in the Si substrate is adjacent to the steep increase as the probe transits to the Si<sub>1-x</sub>Ge<sub>x</sub> and Ge layer with a high density of misfit dislocations. This is followed by a decrease and roughly constant signal in the what is believed to be dislocation-free Ge layer. Finally, as the tip enters the Ge<sub>0.9</sub>Sn<sub>0.1</sub> layer, the heat resistance increases again continuing to increase towards the sample surface suggesting increase of Sn concentration. We exclude the possibility that the thermal resistance variations have their origin at tip-sample contact area variation, since we don't observe any significant topography variations in the cross-sectioned area (see Supplementary Information note 7 for relevant profiles).

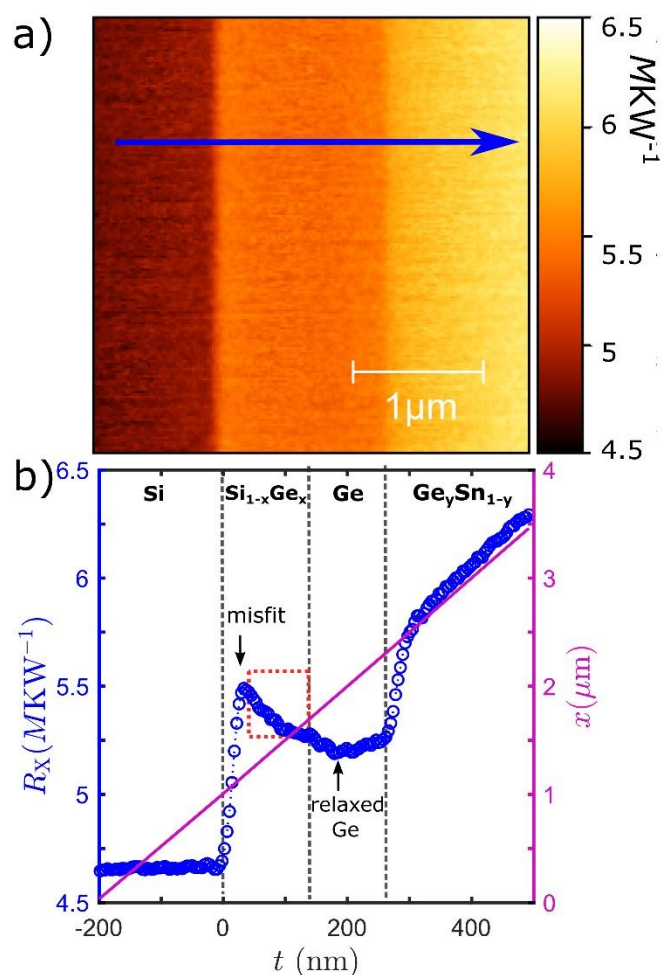


**Fig. 2.** (a) Thermal contact resistance  $R_X$  image across cross-sectioned Si/Ge/Si<sub>x</sub>/Ge<sub>y</sub>Sn<sub>1-y</sub> layers. Image is a zoom in the area shown in Fig. 1b. (b)  $R_X$  profile acquired from the image (blue, left axis), as indicated by the blue arrow by averaging 100 lines, and topography profile,  $x$ , (magenta, right axis) as a function of height,  $t$ , across Si/Ge/Si<sub>x</sub>/Ge<sub>y</sub>Sn<sub>1-y</sub> layers. The areas of different materials are shown and are aligned with the image. The red dotted line denotes an area where dislocation density reduces as moving away from the interface.

The most remarkable observation is that the resistance in the  $\text{Ge}_x\text{Si}_{1-x}$  is decreased in the middle region (red dotted area in Fig. 2) which is consistent with the thermal conductivity of  $\text{Ge}_x\text{Si}_{1-x}$  increase with the decrease of Si content.<sup>30</sup> This significant continuing drop in the thermal resistance extending to 200 nm thickness can be linked with the reduction of the dislocation density as one moves away from the interface. According to Second Ion Mass Spectroscopy (SIMS) measurements (see supplementary note 6), the Ge content of the  $\text{Ge}_x\text{Si}_{1-x}$  layer is quickly increasing from 0 to 80% in the first ~25 nm. This region corresponds to the sharp increase measured in the thermal resistance. Beyond the low thermal conductivity of  $\text{Ge}_x\text{Si}_{1-x}$  alloys with more than 10% Ge (compared to the pure silicon one)<sup>30</sup>, such drastic changes in the layer composition are also likely to induce phonon scattering processes and create a low thermal conductivity which translate into a high thermal resistance increase. Then, between 25 and 125 nm, the Ge content increases slowly from 80% to 90% in the remaining of the layer where the thermal resistance decrease is observed. The thermal conductivity of  $\text{Ge}_x\text{Si}_{1-x}$  alloys increases with Ge content above 80% Ge. We can then attribute the thermal resistance decrease to this increasing thermal conductivity with thickness. In the Ge only layer, our measurement outputs an even lower resistance. This can also be linked to the Ge content that reaches 100% in this region (see supplementary notes 6) and thus provides a higher thermal conductivity.

We then investigated two  $\text{SiGe}_x/\text{GeSn}_y$  samples that have similar composition but different processing conditions, that are known to change the metastable GeSn alloys<sup>26-28</sup> composition and their crystallinity upon annealing at high temperature.<sup>31</sup> Sn mobility inside the Ge can also increase drastically with temperature with Sn atoms tending to form clusters and segregate.<sup>28</sup> To assess these effects, we compared two samples: an as grown sample and a sample that was subsequently annealed at 500°C prior to xSThM characterization. Fig. 3 shows the thermal resistance for these two samples. For comparison purposes, we normalized signals to both the Si and Ge layers which should not change due to the annealing process. Here, we observe almost no difference in the thermal transport in the  $\text{Si}_{1-x}\text{Ge}_x$  region between the as-grown and annealed sample that would be expected, as the annealing temperatures were well below ones needed to anneal SiGe structures. In the pure Ge region, we obtained an almost flat response, which indicates that the spreading resistance is not affected by the increase of Ge layer thickness. When entering the  $\text{Ge}_{0.9}\text{Sn}_{0.1}$  layer, the resistance increases for both samples. This can be expected due to the lower thermal conductivity of GeSn alloys<sup>32, 33</sup> (between 1 and  $10 \text{ Wm}^{-1}\text{K}^{-1}$ ) compared to pure Ge ( $\sim 20 \text{ Wm}^{-1}\text{K}^{-1}$  for 100 nm film<sup>32, 34</sup>). However, a notable difference was observed between the as-grown and the annealed samples by analysis of the absolute value and the derivative of the thermal resistance in these layers. The lower absolute value suggests a higher concentration of Ge near the interface. At the same time, the higher derivative for the annealed sample suggests, similarly to the  $\text{Si}_{1-x}\text{Ge}_x$  region, a different GeSn crystal quality. Annealing is

likely to create clusters of Sn inside the Ge which act as phonon scattering elements, hence reducing the thermal conductivity.

For this complex nanostructure, the xSThM here allowed for the first time to directly link the variation of the local thermal conductance due to the layer composition, crystalline defects and the precipitate nanostructuring, via the physical properties of buried layers that would be impossible to access otherwise. The next section addresses the vital question how to use xSThM for the quantitative thermal measurements in such layers.

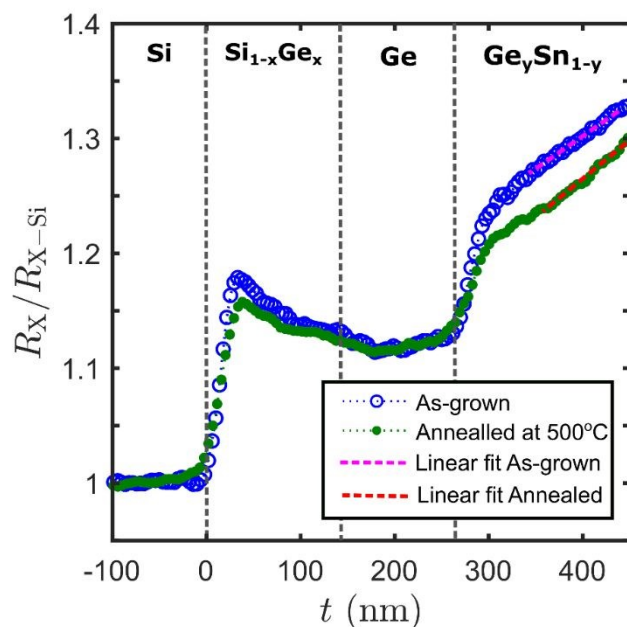


**Fig. 3.** Thermal resistance (normalized with Si and Ge layers thermal resistance) profile as obtained by averaging 100 lines as a function of height for as-grown and annealed samples. With dotted lines the fitted curves of the  $\text{Ge}_y\text{Sn}_{1-y}$  region are indicated. For the as-grown sample the slope is  $dy/dx \approx 5.8 \pm 0.2 \times 10^{-4} \text{ nm}^{-1}$  and for the annealed  $dy/dx \approx 6.9 \pm 0.2 \times 10^{-4} \text{ nm}^{-1}$ .

### Quantitative measurements of thermal conductivity and interfacial thermal resistance

Having established the high performance of thermal transport mapping in 3D layers, we first use xSThM to quantitatively deduce the thermal properties of relatively simple 3D structures comprised of isotropic layers. The wedge-like cut enables SThM measurements as function of material thickness that changes depending on the position of the probe across the cut (see Fig. 4a). As the tip-surface and wedge sample – substrate thermal resistance are independent of the tip position, using samples of varied thicknesses therefore allows to separate the contribution of the interfacial thermal resistance and sample thermal conductivity in order to deduce quantitative properties.<sup>35–39</sup>

For the quantification of the thermal properties, we express  $R_X$  as a sum of two main components connected in series: the total contact thermal resistance between the probe and the sample,  $R_c$ , and the total thermal spreading resistance within the sample,  $R_s$ ,

$$R_X = R_c + R_s. \quad (1)$$

In vacuum,  $R_c$  includes solid-solid contact thermal resistance, and in ambient environment, also water meniscus conductance.<sup>40</sup> For the quantitative evaluation of the sample thermal resistance, we treat  $R_c$  as an effective probe-sample interface resistance dependent on the contact area and the sample thermophysical properties, and independent of  $R_s$ . The SThM tip - sample contact area can be approximated<sup>7</sup> by a disk of radius  $a$ , reflecting the solid-solid contact dimensions and when in ambient conditions, may increase due to effect of water meniscus, providing an *effective radius* of thermal contact.

The thermal spreading resistance depends on the nanoscale structure and materials composition of the sample. In the simple case of a bulk isotropic material and a contact radius above the phonon mean free path  $\Lambda$ , the thermal spreading resistance is given by:

$$R_s = \frac{1}{4ka}, \quad (2)$$

where  $k$  is the thermal conductivity of the bulk material. In case of the contact radius much smaller than mean free path, the ballistic approximation can be used.<sup>41</sup> Diffusive transport assumption remains valid if the heat source dimension  $\alpha$  is bigger than  $\Lambda$  meaning that the system Knudsen number ( $Kn = \Lambda/a$ ) is smaller than 1. In our system,  $\Lambda$  is greatly reduced compared to bulk values due to interface scattering and impurities<sup>30</sup>. Except for dislocation free Si where  $\Lambda \sim 300\text{nm}$ <sup>42</sup>,  $\Lambda$  are usually smaller than 50 nm, the typical effective contact radius<sup>32</sup>. In either case, if the contact dimensions or material does not change, the thermal resistance remain constant.

View Article Online  
DOI: 10.1039/D0NR08768H

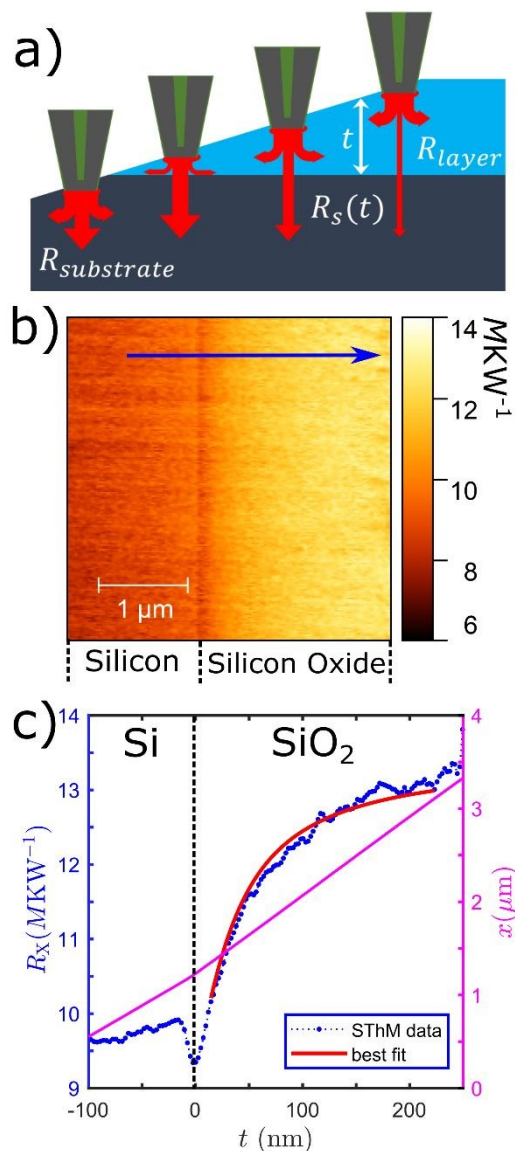


**Fig. 4.** (a) Schematic view of the xSThM scanning along the polished sample with increasing thickness. The arrows show the heat flow direction, with their width denoting the increased heat flow. At the limit of a thick layers heat flow is mostly lateral within the layer. The top surface was removed from the image because it is not nano-sectioned; its roughness is very different from the top surface one, and also the top surface can be contaminated during the sectioning due to re-deposition of material, and these measurements should not be compared directly with the cross-sectioned area in this case (see Supplementary Information Note 8 for the thermal image including the top surface). (b) Thermal contact resistance,  $R_X$ , map of the 300 nm SiO<sub>2</sub> on Si cross-sectioned sample. (c)  $R_X$  profile acquired from the xSThM image by averaging 100 lines as a function of height across Si/SiO<sub>2</sub> layers, in the direction shown by the blue arrow at (b).

The basic element of any 3D nanostructure is a layer with thermal conductivity  $k_1$  on the uniform substrate with thermal conductivity,  $k_s$ . The angle wedge cut through the layer and the substrate, produced by BEXP nano-cross-sectioning, allows us to approximate each measurement point as a layer of variable thickness. We then can use an isotropic model for  $R_s$  for heat spreading within the layer on a substrate as described elsewhere:<sup>43, 44</sup>

$$R_s(t) = \frac{1}{\pi k_1 a} \int_0^\infty \frac{\left[ 1 + K \exp\left(-\frac{2\xi t_{\text{eff}}}{a}\right) \right]}{\left[ 1 - K \exp\left(-\frac{2\xi t_{\text{eff}}}{a}\right) \right]} J_1(\xi) \sin(\xi) \frac{d\xi}{\xi^2} \quad (3)$$

where  $t_{\text{eff}} = t + r_{\text{int}} * k_1$  is the effective thickness that depends on the interfacial resistance between the layer and the substrate per unit area,  $r_{\text{int}}$ , and the layer thickness,  $t$ ,  $J_1$  is the first Bessel function of the first kind,  $\xi$  an integration factor and where  $K$  is defined as  $K = (1 - k_s/k_1)/(1 + k_s/k_1)$ . Note that this model can be extended to orthotropic system<sup>45</sup> to describe thermally anisotropic materials. This thickness varying thermal spreading resistance is connected with the variation in the direction of heat flow as layer thickness crosses from  $t \ll a$  to  $t \gg a$  as schematically represented in Fig. 4a. At the limit of a thick layer with  $t \gg a$ , the spreading resistance will be described by Equation 2.

We investigated three films of standard materials currently widely used in the semiconductor industry<sup>46, 47</sup> with potential for the next generation extreme UV (eUV) lithography: 60 nm spin-on carbon, 10 nm spin-on glass, complemented by the 300 nm thermally grown SiO<sub>2</sub> on a Si substrate. In a BEXP section, thickness of the layer linearly varies with the position and can be precisely quantified via topography.<sup>21</sup> Most significantly, owing to the perfect near-atomic flatness of the cut, the tip-sample thermal resistances as well as the layer-substrate interfacial thermal resistance are constant and do not depend on the layer thickness. This allows us to perform direct fitting of the  $R_x$  vs  $t$  dependence using Equation 3, and therefore independently determine  $k_1$  and  $r_{\text{int}}$ .

Fig. 4b shows the xSThM  $R_x$  map of a 300 nm thermal oxide on Si with thermal resistance of Si area lower than that of SiO<sub>2</sub> as expected.<sup>48</sup> In Fig. 4c, a topography and thermal resistance profiles taken along the blue arrow in Fig. 4b. Thermal resistance of Si is almost stable while for SiO<sub>2</sub> we observe a clear increase with increasing thickness corresponding to an increasing spreading resistance. A narrow dip at the Si-SiO<sub>2</sub> interface is attributed to the topographical variations at the interface that locally changes the contact area between the tip apex and the surface. These can occur at the junctions of the very dissimilar materials, but are not present as we can see in the uniform or smooth gradient materials. These topographical changes can be readily observed and eliminated from the measurements, or compensated by the special algorithms<sup>49</sup>. Note, that the difference of Si thermal resistance with the sample presented in Fig. 2 is due to different tip apex radius, of the probe used. When the probe is solely in contact with the oxide layer, we can assume that the total tip-surface contact resistance  $R_c$  of Equation 1 is constant as material and contact area are not varied. We then apply the analytical model of Equation 3 using unknown parameters  $R_c$ ,  $a$ ,  $k_1$  and  $r_{\text{int}}$  as fitting parameters (see Table 1 for the fitting results). The fitting parameters can be further reduced by defining a new fitting function  $f(t - t_0) = R_s(t) - R_s(t_0)$  and removing in this way the  $R_c$  contribution. However, it can be obtained afterwards by simply finding the offset to match the measured resistance (see

Supplementary information for more details). The independent determination of several independent thermal parameters in a single experiment becomes possible as the measurements are performed for the varied thickness of the sample, that is equivalent of the multiple experiments on the same the system.<sup>39</sup> This approach is effective if we assume that the layer thickness does not affect its thermal conductivity, and that layer thermal conductivity is isotropic (see Supporting Information for more details).

Additionally, we can use the 300 nm oxide sample as a proxy to an “infinitely thick” calibration sample allowing to determine the contact radius  $a$ . By assuming literature values for the SiO<sub>2</sub> thermal conductivity ( $k_{\text{SiO}_2} \approx 1 \text{ W m}^{-1} \text{ K}^{-1}$ )<sup>50, 51</sup> and the interfacial thermal resistance between silicon oxide and silicon ( $r_{\text{int}_{\text{Si-SiO}_2}} \approx 1 \times 10^{-9} \text{ Km}^2 \text{ W}^{-1}$ )<sup>50, 52</sup>, this value only weakly affects the fitting result given the large thickness of the calibration layer) the only fitting parameter is  $a$ . We obtained  $a = 56 \text{ nm}$ , that is reasonable for the SThM probes used, with a good fit quality (see Fig. 4b). We note that all three samples were thermally imaged sequentially under same geometrical settings and the same SThM probe, and therefore no significant change in  $a$  is expected from sample to sample

As Equation 3 is valid for all values of layer thickness, the power of our method also relies on its ability to measure very thin layers. By effectively expanding the thickness scale by 5 times and hence the thickness resolution, it allows us to study physical properties of nanoscale layers that are only few nm thick. Such thin layers are impossible to be addressed by vertical cross-section due to the SThM tip diameter.<sup>21</sup> Applying the same method and using the calibrated effective contact radius, we measured thermal conductivities and the interfacial resistances of 60 nm spin-on carbon, 10 nm spin-on glass (see Table 1). We note a general agreement of a trend between the values is obtained, as spin-on carbon is expected to be more thermally conductive than spin-on glass. Experimental data and fitted curves are available in the Supporting Information (Supporting Note 4).

**Table 1.** Parameters obtained by fitting Eq. 1 to experimental data. For SiO<sub>2</sub>, literature values are used to obtain  $a$  and  $r_{\text{int}}$ . Grey shaded cells are assumed values with contact radius for the probe for spin-on-carbon and spin-on glass taken from the SiOx calibration measurements.

Fitting parameters	300 nm thermal SiOx	60 nm spin-on carbon	10 nm spin-on glass
$k_1$ ( $\text{Wm}^{-1} \text{K}^{-1}$ )	1.0	0.8 ± 0.1	0.3 ± 0.1
$r_{\text{int}}$ ( $10^{-9} \times \text{Km}^2 \text{W}^{-1}$ )	1.0	4 ± 2	2 ± 2
$R_c$ ( $10^6 \times \text{KW}^{-1}$ )	9.0 ± 0.1	5.3 ± 0.1	6.0 ± 0.2
$a$ (nm)	56	56	56

Finally, it is also possible to quantify thermal conductance anisotropy of more complicated gradient structures with the use of FEA. In this context, we studied  $\text{Si}_x\text{Ge}_{1-x}$  gradient material, a good candidate for high temperature thermoelectrics. We found that as the SThM probe scans across different layers of increased Ge concentration, the thermal resistance at the tip apex increases in good agreement with previous studies on  $\text{Si}_{1-x}\text{Ge}_x$  alloys.<sup>30</sup> Modelling the  $\text{Si}_x\text{Ge}_{1-x}$  by FEA enabled us to reproduce experimentally acquired thermal resistance as function of the Ge concentration (see SI Supporting Note 2 for details).

## Conclusions

Combining an SPM compatible nano-cross-sectional tool with SThM, we were able to map and measure with nanoscale resolution the thermal conductivity and interfacial thermal resistance of buried layers and interfaces in complex gradient compound semiconductor nanostructures that were not accessible previously. We applied a new approach to the investigation of thermal conductance of nanomaterials providing depth profiling of thermophysical properties with a depth resolution below 10 nm. We have directly measured heat transport in nano-layered anisotropic systems such as potential optoelectronic  $\text{Si}/\text{Si}_x\text{Ge}_{1-x}/\text{Ge}/\text{Ge}_y\text{Sn}_{1-y}$  and thermoelectric  $\text{Si}_x\text{Ge}_{1-x}$  materials showing excellent match with the theoretical data with no fitting parameters, and observing composition variations and dislocation impeded thermal transport in nanoscale thin layers. Furthermore, using a complimentary modelling approach, we can deduce quantitative values of thermal conductivity in microelectronic thin films and molecular beam epitaxy layers for next generation optoelectronics and thermoelectrics. Our work demonstrates the ability to differentiate between thermal conductivity and interfacial thermal resistance in these samples, and to explore local stoichiometry and crystalline defects in nanostructured materials and devices. This approach could prove to be vitally important for quantitative nanoscale thermal characterization aspects that are currently largely missing in nanomanufacturing.

## Author Contributions

O.K., J.S. and B.R. conceived the idea of the approach and its application. J.S. performed the measurements, data analysis and modelling. C.E. performed vacuum experiments. L.H. and A.R. prepared the sample with BEXP and helped with the experiments. L.H., M.O. and J.S. grew the SiGeSn samples and provided insights on the sample structure and behavior. M.A. ○ and M.G. ○ prepared SiGe samples. A.S., F.A., and C.S. provided samples and interpretation of thermal properties of SiGe. O.K., J.S., E.C provided interpretation of the experimental data and theoretical analysis. J.S. drafted the manuscript, O.K., C.E. revised it and all authors contributed to its final version.

## Conflicts of interest

There are no conflicts to declare.

View Article Online  
DOI: 10.1039/D0NR08768H

## Acknowledgements

The authors acknowledge EU QUANTIHEAT FP7 project no. 604668 and Horizon 2020 Graphene Flagship Core 3 project, EPSRC EP/G015570/1 EP/K023373/1, EP/G06556X/1. EP/V00767X/1 and EP/P006973/1 for overall support, and Paul Instrument Fund, c/o The Royal Society grant on “Infrared non-contact atomic force microscopy (ncAFM-IR)” for the equipment support. We are also grateful to our industrial collaborators Leica Microsystems, Lancaster Materials Analysis Ltd, and Bruker for financial and instrumentation support. LTD to ICN2 is supported by Spanish MINECO (Severo Ochoa Centers of Excellence Program under Grant SEV-2017-0706), and by the Generalitat de Catalunya (Grant 2017SGR806 and the CERCA Program). We thank Severine Gomès from CNRS, and Harry Hoster from Lancaster Energy for helpful discussions on the measurements, and Andy Cockburn and Mike Kocsic from IMEC, for interesting materials and discussion of applications.

## Notes and references

1. C. A. Mack, *IEEE Transactions on Semiconductor Manufacturing*, 2011, **24**, 202-207.
2. A. Majumdar, *Nat Nano*, 2009, **4**, 214-215.
3. S. W. Fong, C. M. Neumann and H. P. Wong, *IEEE Transactions on Electron Devices*, 2017, **64**, 4374-4385.
4. S. Volz, *Microscale and nanoscale heat transfer*, Springer, 2007.
5. H. J. Jang, C. R. Ryder, J. D. Wood, M. C. Hersam and D. G. Cahill, *Advanced Materials*, 2017, **29**.
6. W. Jeong, S. Hur, E. Meyhofer and P. Reddy, *Nanoscale and Microscale Thermophysical Engineering*, 2015, **19**, 279-302.
7. S. Gomès, A. Assy and P.-O. Chapuis, *physica status solidi (a)*, 2015, **212**, 477-494.
8. M. E. Pumarol, M. C. Rosamond, P. Tovee, M. C. Petty, D. A. Zeze, V. Falko and O. V. Kolosov, *Nano Letters*, 2012, **12**, 2906-2911.
9. L. Shi and A. Majumdar, *Journal of Heat Transfer-Transactions of the Asme*, 2002, **124**, 329-337.
10. V. V. Gorbunov, N. Fuchigami, J. L. Hazel and V. V. Tsukruk, *Langmuir*, 1999, **15**, 8340-8343.
11. K. Luo, R. W. Herrick, A. Majumdar and P. Petroff, *Applied Physics Letters*, 1997, **71**, 1604-1606.
12. T. Lee, X. Guo, G. Shen, Y. Ji, G. Wang, J. Du, X. Wang, G. Gao, A. Altes and L. Balk, *Microelectronics Reliability*, 2002, **42**, 1711-1714.
13. K. W. Park, E. M. Krivoy, H. P. Nair, S. R. Bank and E. T. Yu, *Nanotechnology*, 2015, **26**, 265701.
14. J. Juszczak, M. Krzywiecki, R. Kruszka and J. Bodzenta, *Ultramicroscopy*, 2013, **135**, 95-98.
15. E. Jung, G. Hwang, J. Chung, O. Kwon, J. Han, Y.-T. Moon and T.-Y. Seong, *Applied Physics Letters*, 2015, **106**, 041114.
16. D. Choi, N. Poudel, S. Park, D. Akinwande, S. B. Cronin, K.

- Watanabe, T. Taniguchi, Z. Yao and L. Shi, *Acs Applied Materials & Interfaces*, 2018, **10**, 11101-11107.
17. J. L. Bosse, I. Grishin, B. D. Huey and O. V. Kolosov, *Applied Surface Science*, 2014, **314**, 151-157.
18. O. V. Kolosov, I. Grishin and R. Jones, *Nanotechnology*, 2011, **22**, 185702.
19. O. V. Kolosov and I. Grishin, *Journal*, 2015.
20. A. J. Robson, I. Grishin, R. J. Young, A. M. Sanchez, O. V. Kolosov and M. Hayne, *ACS Appl Mater Interfaces*, 2013, **5**, 3241-3245.
21. A. J. Robson, I. Grishin, R. J. Young, A. M. Sanchez, O. V. Kolosov and M. Hayne, *Acs Applied Materials & Interfaces*, 2013, **5**, 3241-3245.
22. P. S. Dobson, G. Mills and J. M. R. Weaver, *Review of Scientific Instruments*, 2005, **76**.
23. P. Tovee, M. E. Pumarol, D. A. Zeze, K. Kjoller and O. Kolosov, *J. Appl. Phys.*, 2012, **112**, 114317.
24. C. Evangeli, J. Spiece, S. Sangtarash, A. J. Molina-Mendoza, M. Mucientes, T. Mueller, C. Lambert, H. Sadeghi and O. Kolosov, *Advanced Electronic Materials*, 2019, **5**.
25. J. Spiece, C. Evangeli, K. Lulla, A. Robson, B. Robinson and O. Kolosov, *Journal of Applied Physics*, 2018, **124**, 015101.
26. N. Bhargava, J. P. Gupta, N. Faleev, L. Wielunski and J. Kolodzey, *Journal of Electronic Materials*, 2017, **46**, 1620-1627.
27. W. Wang, L. Li, Q. Zhou, J. Pan, Z. Zhang, E. S. Tok and Y.-C. Yeo, *Applied Surface Science*, 2014, **321**, 240-244.
28. L. Kormoš, M. Kratzer, K. Kostecky, M. Oehme, T. Šikola, E. Kasper, J. Schulze and C. Teichert, *Surface and Interface Analysis*, 2017, **49**, 297-302.
29. M. Oehme, D. Buca, K. Kostecky, S. Wirths, B. Holländer, E. Kasper and J. Schulze, *Journal of crystal growth*, 2013, **384**, 71-76.
30. A. Iskandar, A. Abou-Khalil, M. Kazan, W. Kassem and S. Volz, *Journal of Applied Physics*, 2015, **117**, 125102.
31. H. Mahmodi and M. R. Hashim, *Materials Research Express*, 2016, **3**, 106403.
32. S. N. Khatami and Z. Aksamija, *Physical Review Applied*, 2016, **6**.
33. N. Uchida, T. Maeda, R. R. Lieten, S. Okajima, Y. Ohishi, R. Takase, M. Ishimaru and J.-P. Locquet, *Applied Physics Letters*, 2015, **107**, 232105.
34. R. Cheaito, J. C. Duda, T. E. Beechem, K. Hattar, J. F. Ihlefeld, D. L. Medlin, M. A. Rodriguez, M. J. Campion, E. S. Piekos and P. E. Hopkins, *Phys Rev Lett*, 2012, **109**, 195901.
35. A. Makris, T. Haeger, R. Heiderhoff and T. Riedl, *RSC Adv.*, 2016, **6**, 94193-94199.
36. R. Heiderhoff, H. Li and T. Riedl, *Microelectronics Reliability*, 2013, **53**, 1413-1417.
37. S. Gome, L. David, V. Lysenko, A. Descamps, T. Nychyporuk and M. Raynaud, *Journal of Physics D-Applied Physics*, 2007, **40**, 6677-6683.
38. J. Juszczak, A. Kazmierczak-Balata, P. Firek and J. Bodzenta, *Ultramicroscopy*, 2017, **175**, 81-86.
39. J. L. Bosse, M. Timofeeva, P. D. Tovee, B. J. Robinson, B. D. Huey and O. V. Kolosov, *Journal of Applied Physics*, 2014, **116**, 134904.
40. A. Assy and S. Gomes, *Nanotechnology*, 2015, **26**, 355401.
41. R. Prasher, *Nano Letters*, 2005, **5**, 2155-2159.
42. K. T. Regner, D. P. Sellan, Z. Su, C. H. Amon, A. J. H. McGaughey and J. A. Malen, *Nature Communications*, 2013, **4**, 1640.
43. Y. S. Muzychka, M. M. Yovanovich and J. R. Culham, *J. Thermophys Heat Transfer*, 2004, **18**, 45-51.
44. Y. S. Muzychka, *Journal of Thermophysics and Heat Transfer*, 2014, **28**, 313-319.
45. F. Menges, H. Riel, A. Stemmer, C. Dimitrakopoulos and B. Gotsmann, *Phys Rev Lett*, 2013, **111**, 205901.
46. A. Frommhold, R. E. Palmer and A. P. Robinson, *Journal of Micro/Nanolithography, MEMS, and MOEMS*, 2013, **12**, 033003-033003.
47. A. Frommhold, J. Manyam, R. E. Palmer and A. P. G. Robinson, *Microelectronic Engineering*, 2012, **98**, 552-555.
48. B. Deng, A. Chernatynskiy, M. Khafizov, D. H. Hurley and S. R. Phillpot, *Journal of Applied Physics*, 2014, **115**, -.
49. P. Klapetek, J. Martinek, P. Grolich, M. Valtr and N. J. Kaur, *Int. J. Heat Mass Transfer*, 2017, **108**, 841-850.
50. A. Al Mohtar, G. Tessier, R. Ritasalo, M. Matvejeff, J. Stormonth-Darling, P. Dobson, P. Chapuis, S. Gomès and J. Roger, *Thin Solid Films*, 2017, **642**, 157-162.
51. K. Goodson, M. Flik, L. Su and D. Antoniadis, *Journal of Heat Transfer*, 1994, **116**, 317-324.
52. J. Chen, G. Zhang and B. Li, *Journal of Applied Physics*, 2012, **112**, 064319.